Flow Structures in a U-Shaped Fuel Cell Flow Channel: Quantitative Visualization Using Particle Image Velocimetry

J. Martin

P. Oshkai

N. Djilali

Institute for Integrated Energy Systems and
Department of Mechanical Engineering,
University of Victoria, PO Box 3055 STN CSC,
Victoria, BC V8W 3P6, Canada

Flow through an experimental model of a U-shaped fuel cell channel is used to investigate the fluid dynamic phenomena that occur within serpentine reactant transport channels of fuel cells. Achieving effective mixing within these channels can significantly improve the performance of the fuel cell and proper understanding and characterization of the underlying fluid dynamics is required. Classes of vortex formation within a U-shaped channel of square cross section are characterized using high-image-density particle image velocimetry. A range of Reynolds numbers, $109 \leqslant Re \leqslant 872$, corresponding to flow rates encountered in a fuel cell operating at low to medium current densities is investigated. The flow fields corresponding to two perpendicular cross sections of the channel are characterized in terms of the instantaneous and time-averaged representations of the velocity, streamline topology, and vorticity contours. The critical Reynolds number necessary for the onset of instability is determined, and the two perpendicular flow planes are compared in terms of absolute and averaged velocity values as well as Reynolds stress correlations. Generally, the flow undergoes a transition to a different regime when two recirculation zones, which originally develop in the U-bend region, merge into one separation region. This transition corresponds to generation of additional vortices in the secondary flow plane. [DOI: 10.1115/1.1843121]

1 Introduction

In a proton exchange membrane (PEM) fuel cell (FC), the membrane electrode assembly, where the electrochemical reaction and transport processes take place, is typically sandwiched between two bipolar plates, which serve to (a) collect the electric current, and (b) supply the reactants through the embedded flow channels. The operation of a PEMFC depends critically on the effective distribution of air and hydrogen in these flow channels, and on the maintenance of both operating temperature and of well humidified conditions in the membrane. The distribution of reactant gases is particularly critical on the cathode (oxygen) side, which is prone to mass transport limitations. The cathode is usually fed with air at relatively low pressure (1–3 atm). As the electrochemical reaction proceeds, the concentration of oxygen in the airflow channels gradually drops. Because of imperfect mixing, the concentration drop is largest in the vicinity of the electrodes. At high current densities, the rate at which oxygen is supplied from the cathode side to the reaction site (catalyst layer) becomes insufficient and the cell is "starved." This so-called concentration polarization results in a significant drop in the voltage produced by the cell, thus limiting the power output. Effective mixing in the reactant gas flow channels is therefore highly desirable.

The most common channel design on a bipolar plate is a serpentine design, as shown in Fig. 1. Characterization of the fluid dynamics in the serpentine gas flow channels is essential to understanding and improving mixing. So far, the highly reactive environment of a fuel cell has been a major challenge to detailed in situ measurements during operation, and though significant progress has been made in computational modeling, the complexity of the phenomena has required a number of simplifying assumptions, and in particular the flow in these models is assumed steady and laminar [1,2].

Flow in curved pipes and serpentine flow channels are encountered in a number of other engineering systems, particularly in chemical processing and heat exchangers, and such flows have been the subject of numerous experimental and numerical studies. The analytic foundations for secondary flows in curved pipes were laid by Dean [3] who established that the onset of secondary vortices in curved pipes is characterized by the ratio of the Reynolds number to the square of the product of the inertia and centrifugal forces. The nondimensionalized parameter, the Dean number, is $\mathrm{Dn}=\mathrm{Re}/(\mathrm{Rc})^{1/2}$. The Reynolds number is $\mathrm{Re}=Ua/v$, where U is the average velocity, a is the hydraulic diameter, v is the

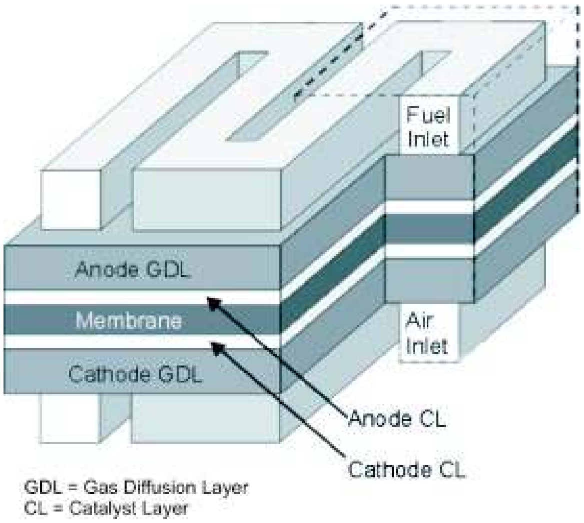

Fig. 1 Schematic of a serpentine gas flow channel

Manuscript received July 27, 2004; revision received August 15, 2004. Review conducted by: N. M. Sammes.

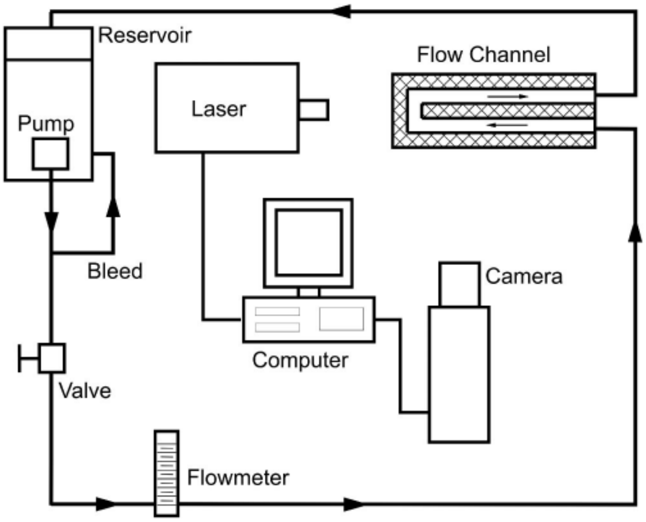

Fig. 2 Schematic of the experimental setup

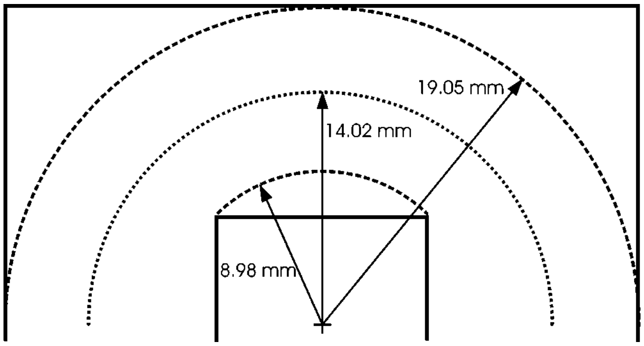

Fig. 4 Estimation of the radius of curvature of the channel

kinematic viscosity, $Rc=R/a$ is the curvature ratio, and R is the radius of curvature.

The secondary (Dean) flow in a curved pipe occurs along the centerline of the tube cross section, from the inner radius towards the outer, before recirculating back along the pipe walls and is attributed to the effect of the centrifugal pressure gradient in the main flow acting on the relatively low momentum fluid in the wall boundary layer. Although Hawthorne [4] showed that the secondary flow could occur in a perfectly inviscid flow as a result of a nonuniform distribution of velocity at the entrance, most work focused on the centrifugal effects. Some of the notable experimental investigations into curved pipe flow include those of Agrawal et al. [5] and Olson and Snyder [6], while Lin and Tarbell [7] also conducted a numerical study. One of the most comprehensive reviews of the numerical and experimental work performed on flows in curved pipes is provided by Berger and Talbot [8].

While pipe flow was the original focus of research of curved channel flows, square and rectangular channels have also received significant attention. Flow in square ducts differs from pipe flow by the onset of additional vortex structures. Since the most common application of curved square and rectangular ducts is in heat exchangers, particularly in turbines, the majority of the investigations involved turbulent flow, and in many cases rotation. Studies of laminar secondary motion in nonrotating curved channels include the experimental and numerical studies of Humphrey et al. [9] and Bara et al. [10]. In a continuation of the work performed by Bara et al., [10] Mees et al. [11] observed the onset of a six-cell secondary flow pattern above a Dean number of 350. An additional pair of vortices also appeared along the outer radius wall. Gauthier et al. [12] did not investigate the secondary flow; but performed a visualization study of the bulk streamwise flow and observed the onset of instability at $Re=340$. The review by Berger

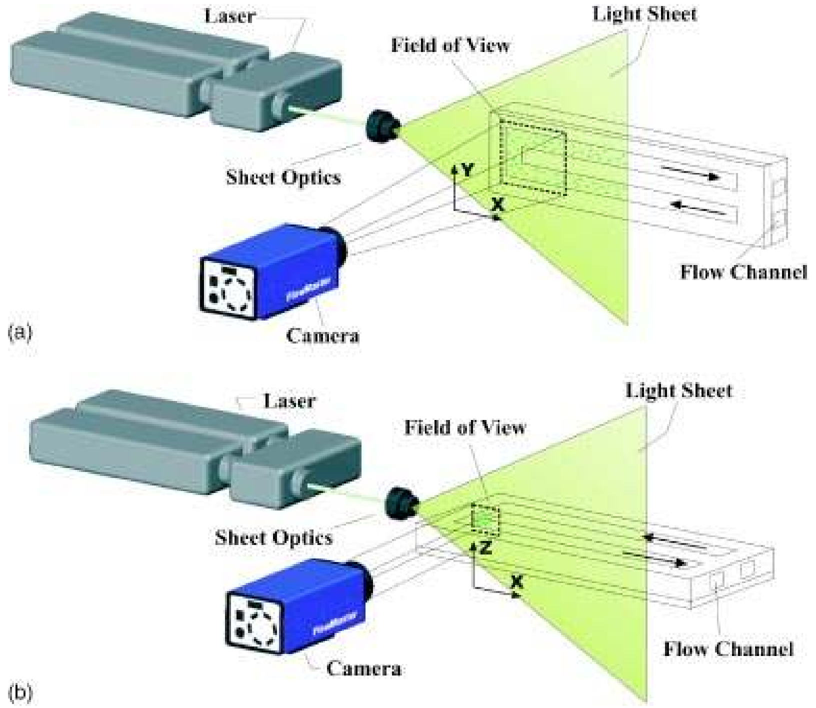

Fig. 3 Schematic of PIV setup for image acquisition in streamwise (*a*) and cross-flow (*b*) planes

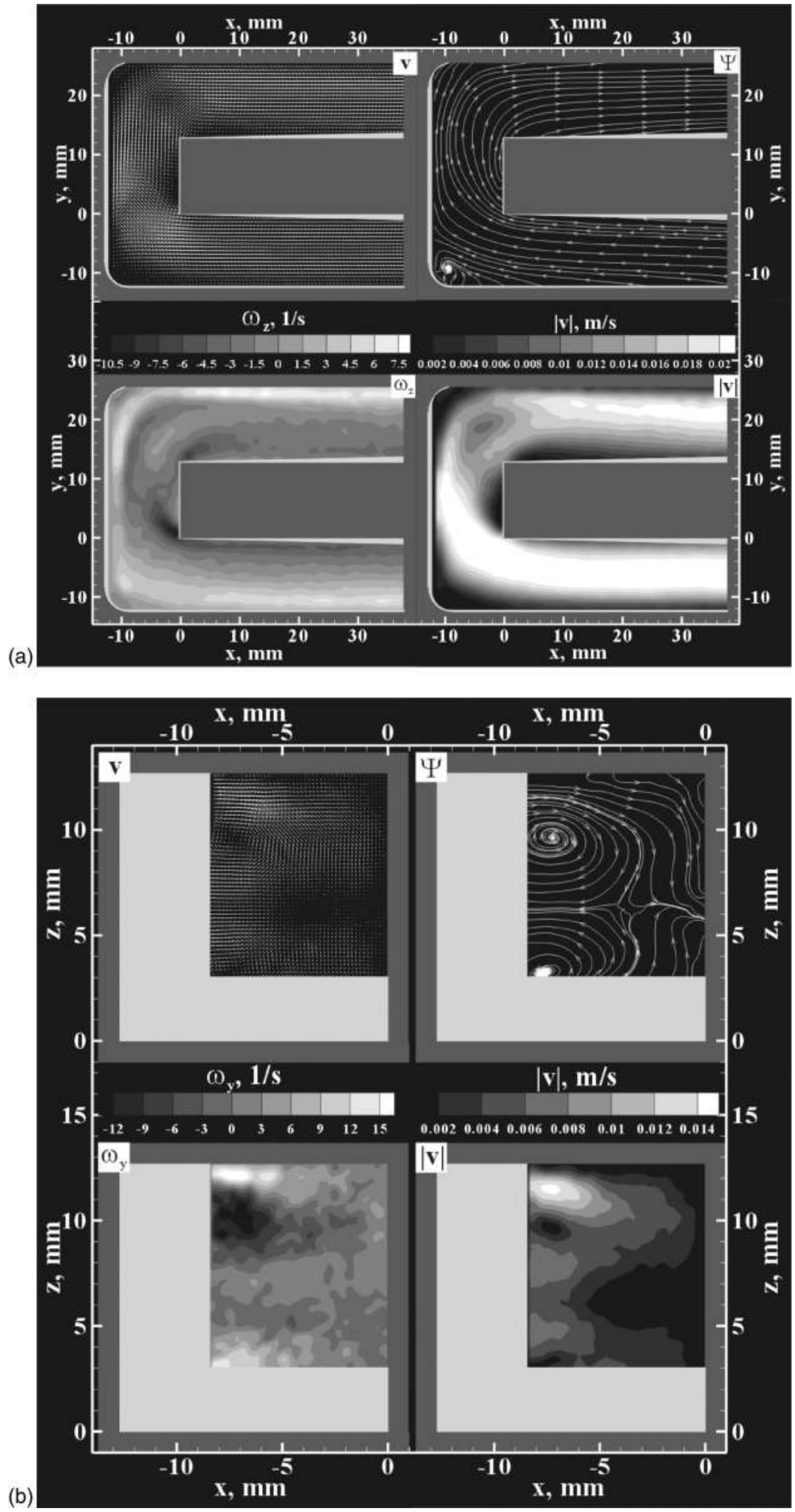

Fig. 5 Instantaneous flow field at Re=109 in streamwise (*a*) and cross-flow (*b*) planes. Clockwise from top left: velocity vector field, velocity streamlines, velocity magnitude, and out-of-plane vorticity contours.

and Talbot [8] also contains significant resources on flows in curved channels of square and rectangular cross-sections.

In fuel cells, the bipolar plate contains serpentine channels that usually more closely resemble a squared U-bend than a curved channel. In a U-bend channel with a 180 deg sharp turn, the flow is also affected by impingement, recirculation, and flow separation. The majority of previous studies related to sharp U-bends are primarily concerned with heat transfer phenomena. Although the literature is dominated by turbulent flow in rotating channels, studies on laminar flow in nonrotating channels are also available. The numerical study by Chintada et al. [13] contains an overview of the flow and heat transfer characteristics,

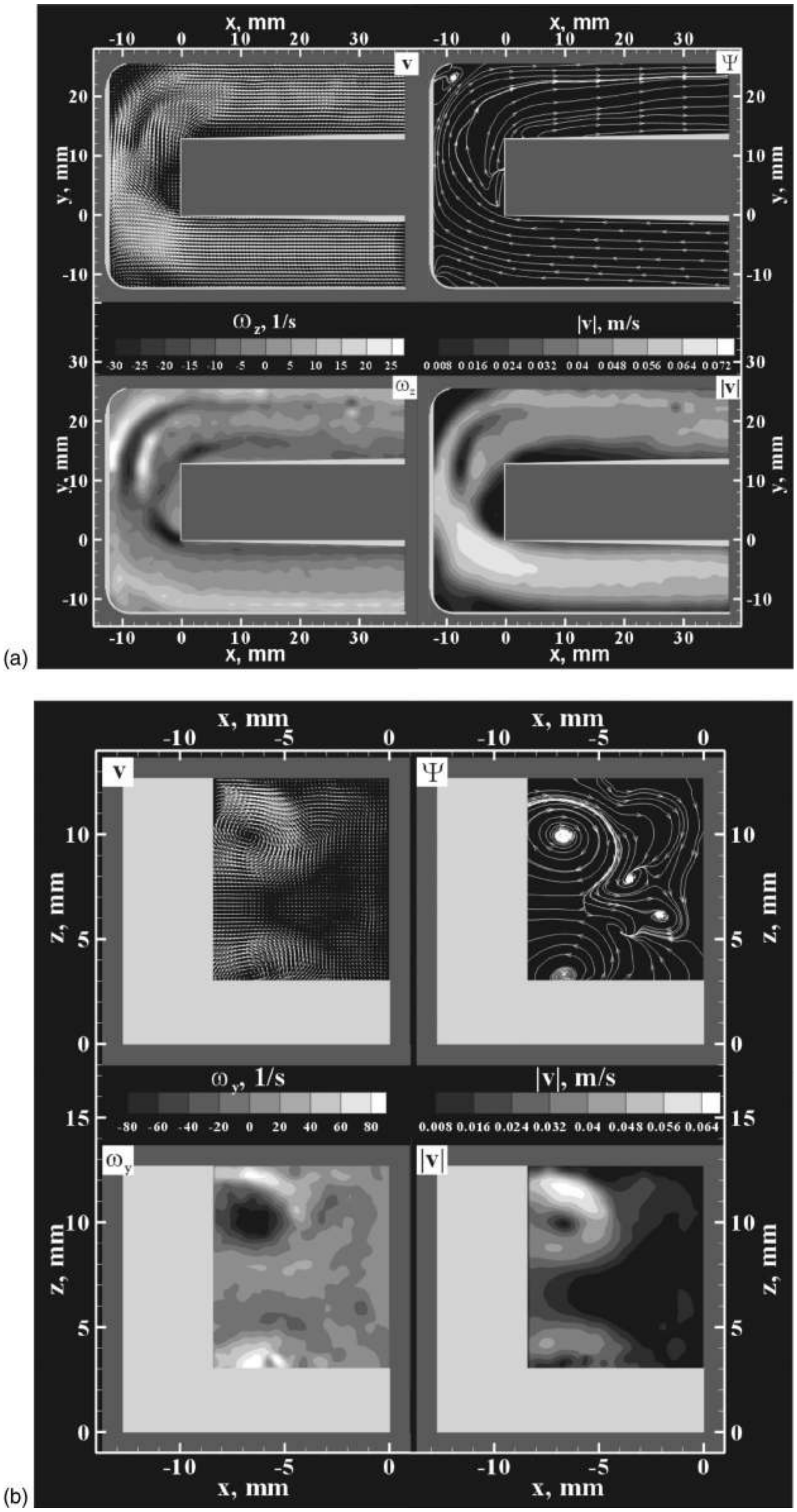

Fig. 6 Instantaneous flow field at Re=382 in streamwise (*a*) and cross-flow (*b*) planes. Clockwise from top left: velocity vector field, velocity streamlines, velocity magnitude, and out-of-plane vorticity contours.

but does not present any detailed analysis of the secondary flow. Mochizuki et al. [14] presented a very clear visualization of the flow during and after a sharp turn at Re=500. Lastly Choi et al. [15] provided a discussion of the onset of instability in laminar flow.

In the present study, the experimental technique of particle imaging velocimetry (PIV) is used to provide a detailed description of the flow in a serpentine flow channel. A 180 deg sharp turn is utilized to simulate the first two passes of a serpentine channel. The flow is characterized in terms of the instantaneous and time-

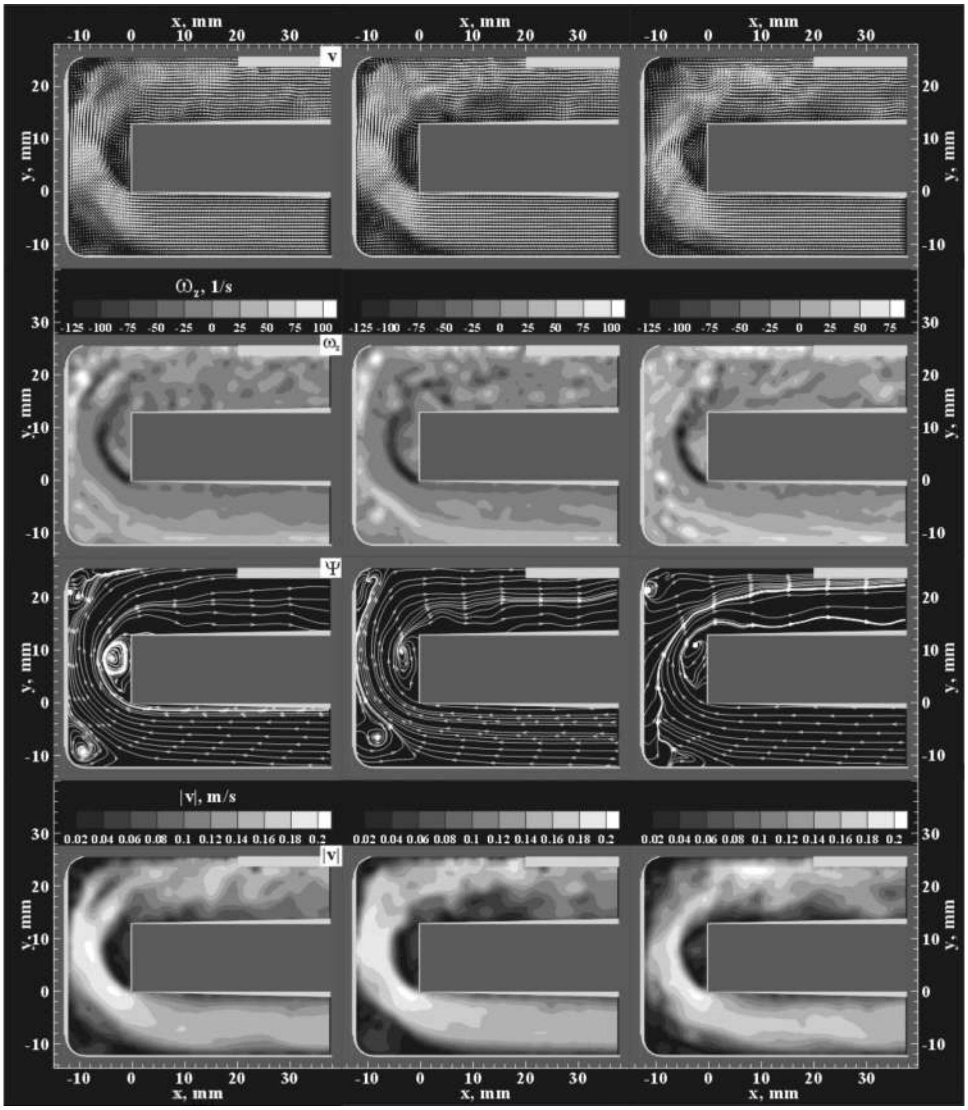

Fig. 7 Streamwise plane: Instantaneous flow fields at Re=872. From top to bottom: velocity vector field, out-of-plane vorticity contours, velocity streamlines, and velocity magnitude.

averaged representations of the velocity, streamline topology, and vorticity contours. These characteristics are used to examine the secondary flow at the midpoint of the turn as well as the onset of instability in laminar flow at increasing Reynolds numbers.

2 Experimental System And Techniques

2.1 Overview of Experimental System. The main components of the experimental setup are shown in Fig. 2. The flow system consisted of a reservoir with a pump, a supply system with a bleed, and a flow channel. Recirculation of the water eliminated the need to constantly resupply the system with seeding particles. The flow channel was made of Plexiglas and had a 12.7 mm square cross section, with a gap of 12.7 mm between the inlet and outlet sections. The distance between the start of the square flow channel and the beginning of the U-bend was 279.4 mm. The PIV system was deployed to acquire data from two major planes of flow. Streamwise and cross-flow planes of image acquisition are shown in Fig. 3.

2.2 Experimental Procedure. Typically, fuel cell current densities do not exceed 1.5 A/cm^2. Above this threshold, which is well past the maximum power density, mass transport constraints cause the voltage to drop sharply. This range of fuel cell current densities corresponds to a range of Re of 0–2077, as determined in the Institute for Integrated Energy Systems Fuel Cell Lab by testing a fuel cell with an active area of 30 cm^2 and a channel width of 0.8 mm. The current study focuses on the range of Re from 0 to 872. Data were collected at flow rates ranging from 5 to 40 lph in 5 lph increments, with an estimated uncertainty of the flow meter of ±1 lph. One hundred pairs of images were acquired at each flow rate, with the time between pairs of images ranging from 297 ms to 3 s. A cross-correlation algorithm was utilized with an initial interrogation region size of 64×64 pixels and a 50% overlap between the adjacent regions in both x and y directions. Subsequent reduction of the interrogation region size during processing resulted in a final resolution of 0.612×0.612 mm in the streamwise plane and 0.209×0.209 mm in the cross-flow plane. Vector post-processing was then used to remove spurious vectors within the flow field.

To further investigate the observed transition in the flow pattern (elaborated upon in the results), an additional data set was collected at 17.5 lph. The data presented herein were collected at flow rates of 5, 17.5, and 40 lph, which correspond to Reynolds numbers of 109, 381, and 872, respectively.

For the purposes of calculating the Dean number, an estimation of the channel curvature was performed as illustrated in Fig. 4.

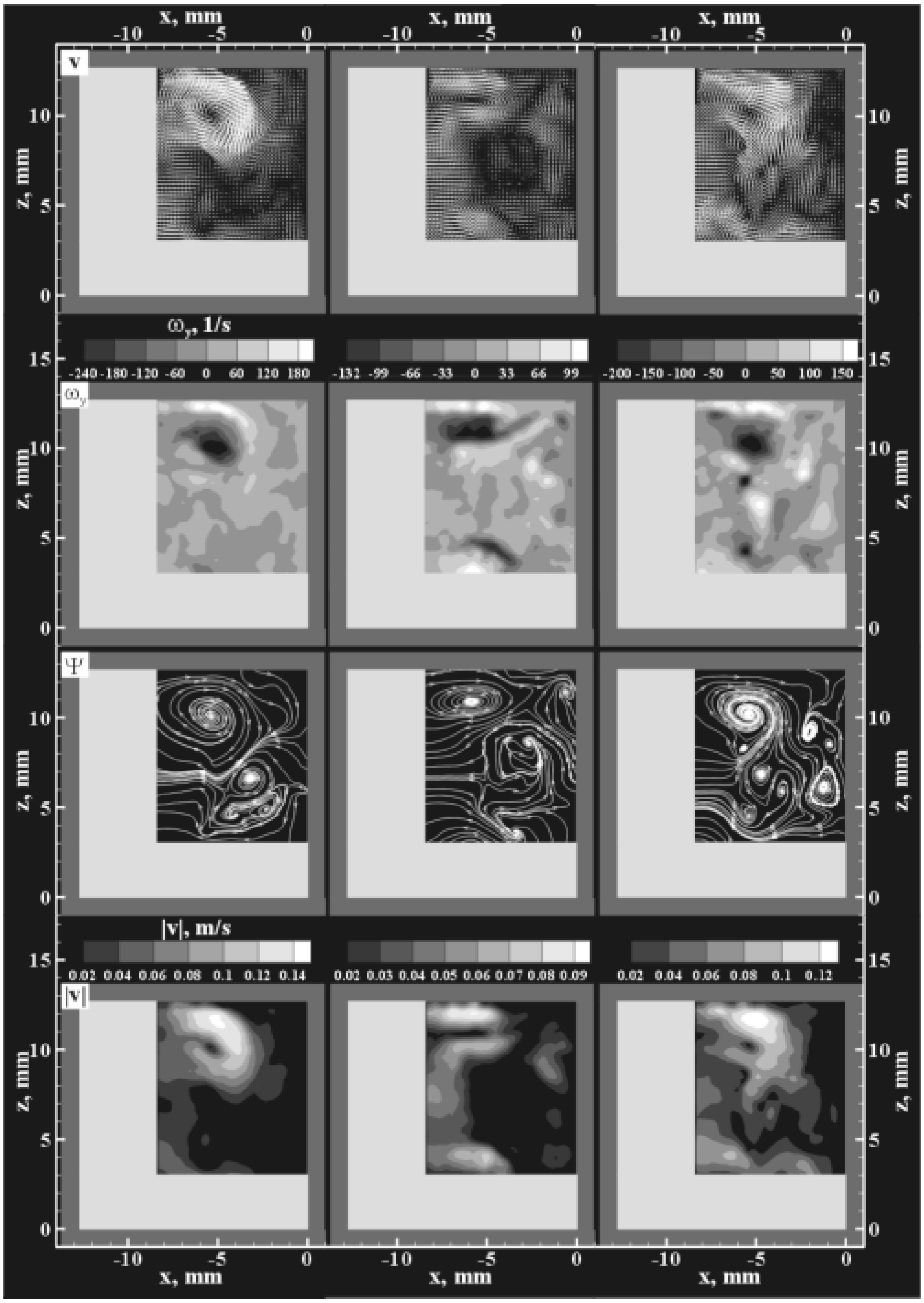

Fig. 8 Cross-flow plane: Instantaneous flow fields at Re=872. From top to bottom: velocity vector field, out-of-plane vorticity contours, velocity streamlines, and velocity magnitude.

With a curvature ratio of 1.1, the Dean numbers corresponding to the three experimental Reynolds numbers are 104, 363, and 831. Due to the flow rate uncertainty, the uncertainty in the Reynolds and Dean numbers range from 2.5% at the highest flow rate to 20% at the low flow rate.

3 Overview of Flow Patterns: Effect of Flow Rate

3.1 Instantaneous Flow Patterns. Various representations of the instantaneous flow field in the U-bend are shown in Figs. 5–8. The images show distributions of instantaneous flow velocity, out-of-plane vorticity, streamline patterns, and velocity magnitude. The shaded gray regions represent locations where no data is available due to optical inaccessibility.

3.1.1 Re=109. Figure 5 shows instantaneous flow patterns at Re=109. The top four plots correspond to the streamwise plane of data acquisition, which is shown schematically in Fig. 3(*a*). The flow enters the U-bend from right to left through the lower section of the channel and exits from right to left through the upper section. Little or no fluctuation is detectable in this low-flow-rate regime. The instantaneous images are essentially identical to the time-averaged flow representations (not presented here), indicating steady flow conditions. Near the top of the U-bend, a low-velocity zone is present in the flow field close to the middle of the channel. It is most prominent in the absolute velocity contour plot. This low-velocity zone is a characteristic feature of the flow in the low Reynolds number regime. The absolute velocity contours also

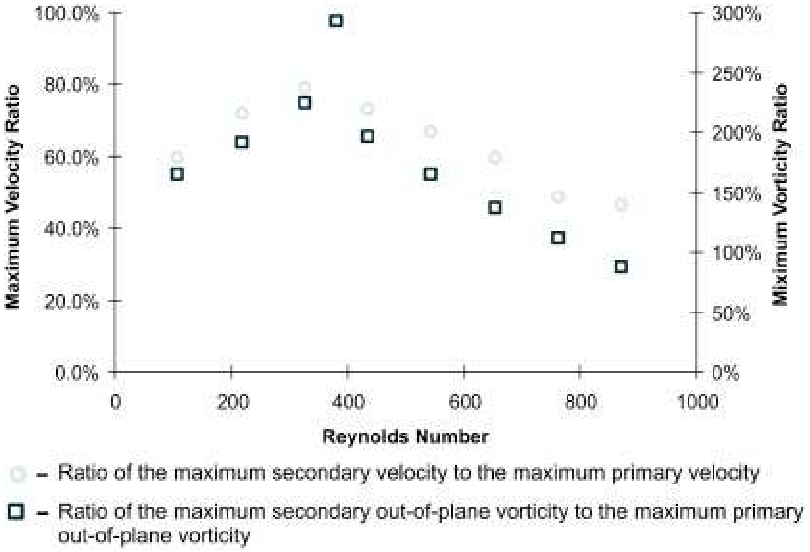

Fig. 9 Ratio of the maximum secondary velocity to the maximum primary velocity and ratio of the maximum secondary out-of-plane vorticity to the maximum primary out-of-plane vorticity as functions of Reynolds number

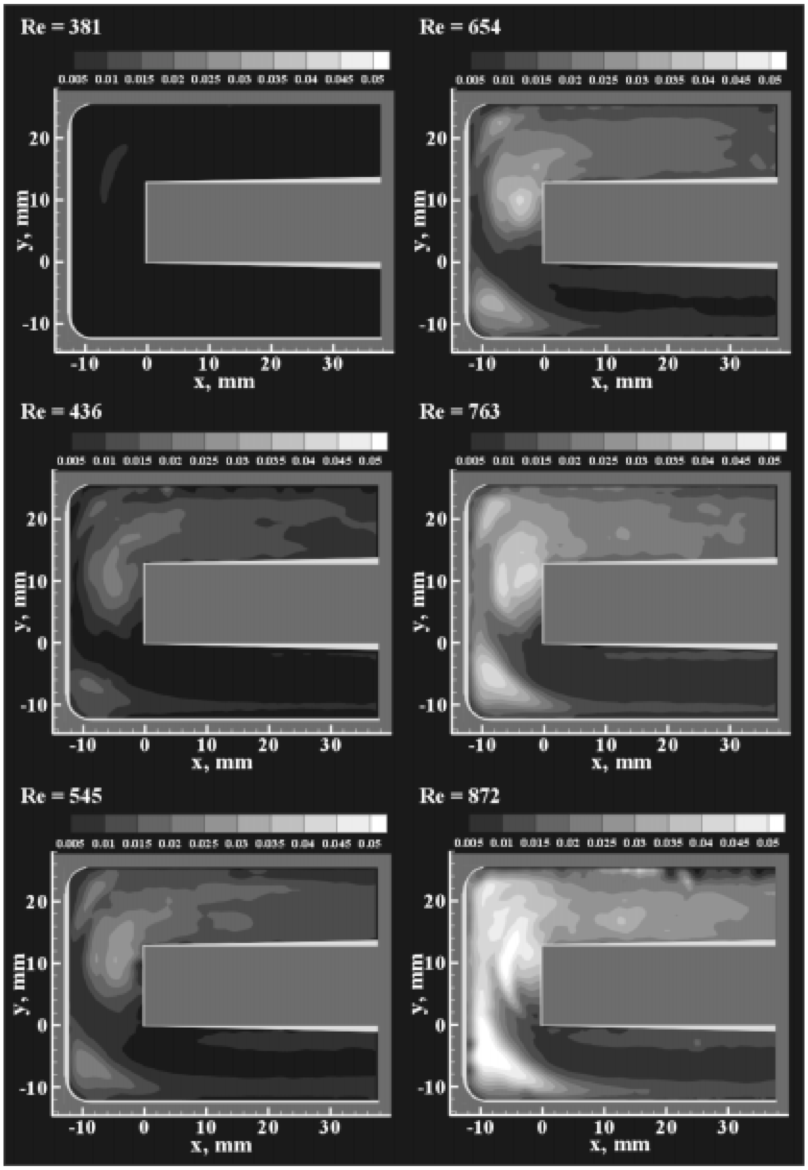

Fig. 10 Patterns of root-mean-square velocity fluctuations in the streamwise plane

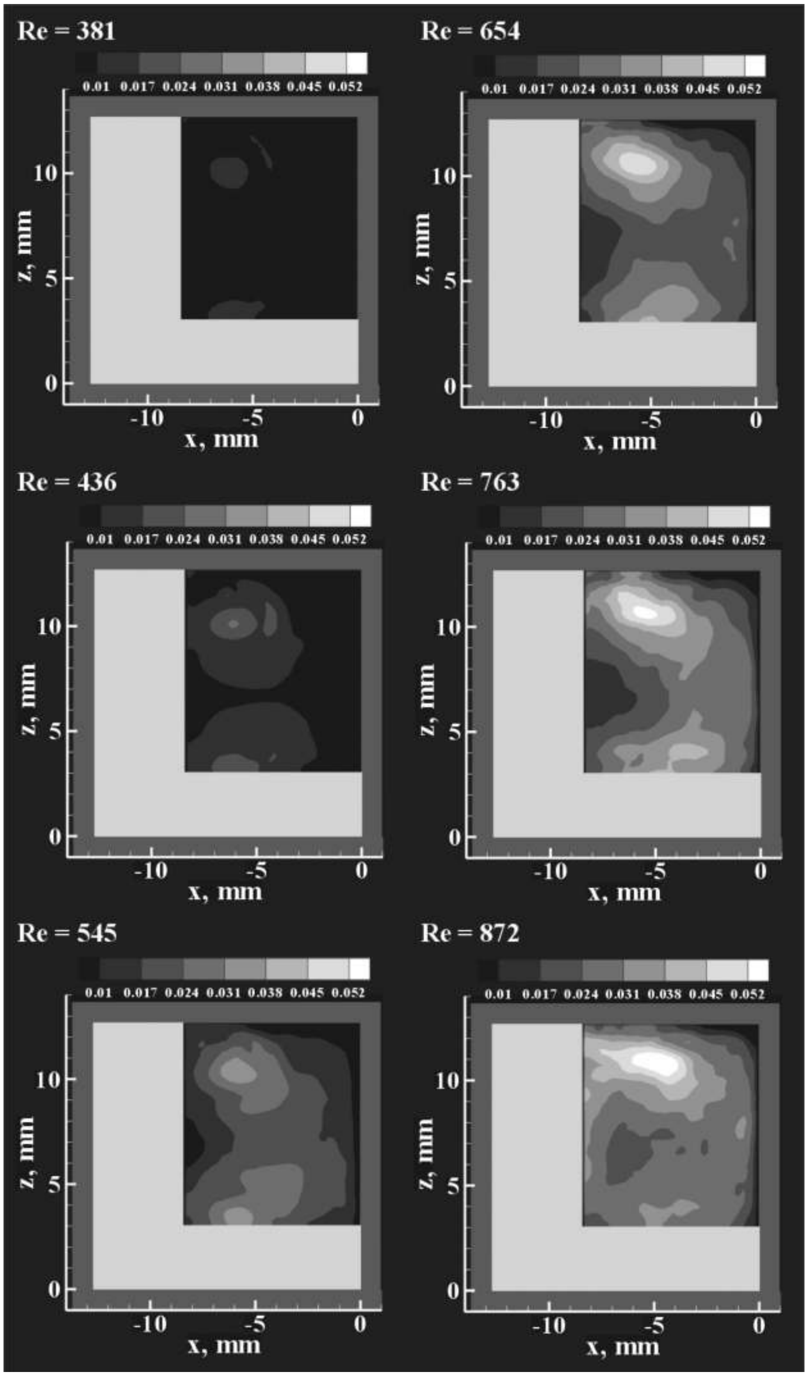

Fig. 11 Patterns of root-mean-square velocity fluctuations in the cross-flow plane

show continued stability of the flow after the bend. The high vorticity regions associated with the formation of separated shear layers from the sharp convex corners of the U-bend are easily detectable in the vorticity contour plot. It should be noted that in the low-flow-rate regime the shear layer that forms at the upstream (bottom) inner corner of the U-bend reattaches to the vertical portion of the inner wall (before the second inner corner). An additional region of high vorticity is associated with the earlier-mentioned low-velocity zone in the middle of the channel.

The bottom four plots correspond to the cross-flow plane of data acquisition, which is represented in Fig. 3(*b*). The primary flow through the channel is directed towards the reader. The expected secondary flow pattern with two symmetric circulation zones (Dean vortices) is clearly exhibited in the velocity vector plot. The vorticity contour plot also shows the onset of the four-vortex structure observed in previous studies of the Dean problem in a square channel [10,11]. The optically inaccessible area makes it impossible to determine if a six-vortex structure is present. The streamline plot and the velocity contour plot provide additional description of the circulation zone structure.

3.1.2 Re = 381. Figure 6 corresponds to the Reynolds number of 381, just prior to the transition to the high-flow-rate regime. The characteristic flow structures that were detected at Re = 109 are still present at Re = 381. In the streamwise plane, the low-velocity zone in the middle of the channel is more pronounced. In

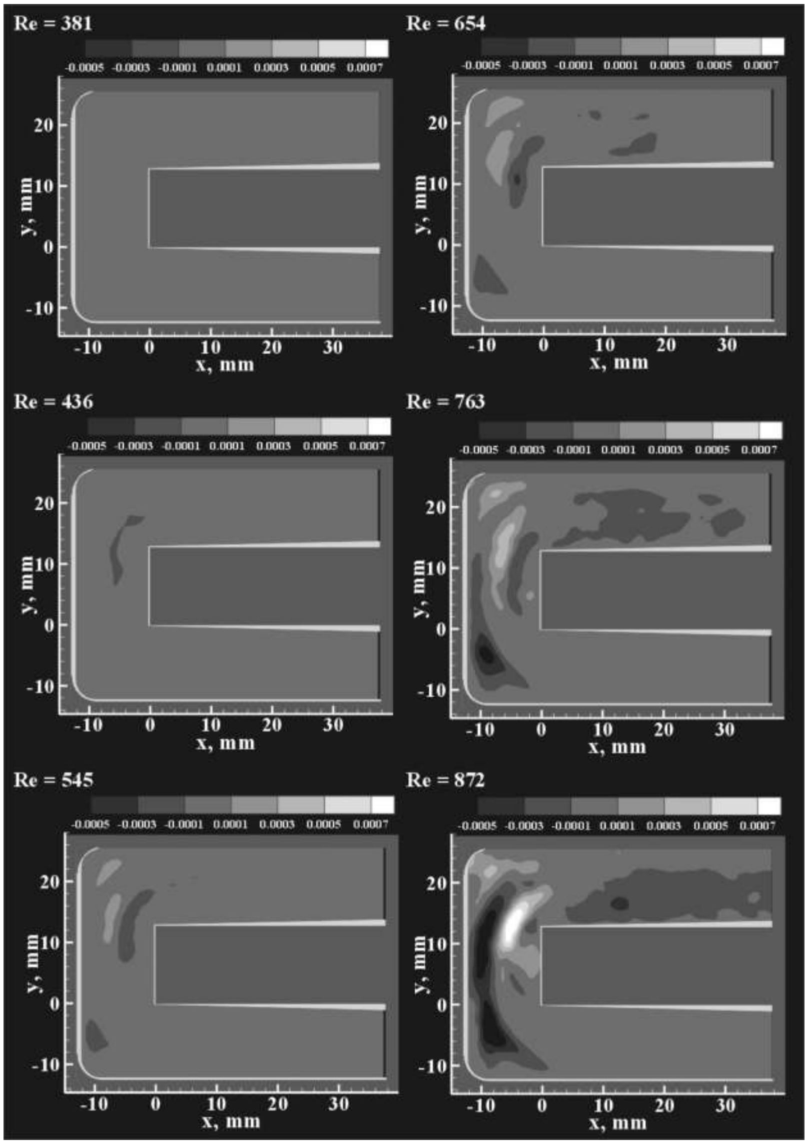

Fig. 12 Patterns of Reynolds stress correlation in the streamwise plane

addition, the reattachment point for the shear layer that is formed at the upstream (bottom) inner corner moves higher along the vertical section of the inner wall, and is now located just prior to the second inner corner. The streamline and vorticity patterns in the portion of the channel just downstream of the U-bend reveal the presence of small-scale flow structures, which serve as indicators of the onset of instability.

The secondary flow patterns in the cross-stream plane, represented by the bottom four plots of Fig. 6, exhibit the same symmetric secondary recirculation zones seen in the lower Reynolds number case. At Re=381, the vorticity contours shows more circular Dean vortices and a more elongated secondary vortex on the top. The Dean vortices have significantly higher values of circulation, as indicated by the higher values of the out-of-plane vorticity. The streamline and absolute velocity contour plots reveal additional small-scale circulation zones that are induced by the stronger Dean vortex pair, and which are not present at the lower Reynolds number case. These features indicate the onset of instability.

3.1.3 Re=872. A transition in the flow regime was observed between the values of Reynolds number of 381 and 436. Figure 7 shows, from top to bottom, plots of velocity distribution, vorticity contours, streamline patterns, and absolute values of velocity in the streamwise plane at a higher Reynolds number of 872. The three columns in Fig. 7 correspond to three representative time instants at this high-flow-rate regime. The flow patterns still exhibit the global features of the low-flow-rate mode, but the flow is now unsteady. The unsteadiness is manifested primarily in the large-scale flow structures, with shrinking and expansion of the low-velocity zone in the middle of the channel at the second turn of the U-bend and the appearance of secondary vortices induced by the recirculating flow in the outer corners of the U-bend. Moreover, the separated shear layer from the first (upstream) inner corner exhibits an unsteady vortex shedding pattern. The flow remains separated from the inner wall past the second corner of the U-bend. The flow remains unsteady for several channel diameters downstream of the U-bend as indicated by the presence of small-scale vortical structures. These small-scale vortices are represented in the streamline plots of Fig. 7 by the wave-like patterns along the inner wall of the channel. Analysis of these patterns can provide quantitative information about the frequency of the observed flow instability and its dependence on the flow rate and channel geometry.

Figure 8 shows the secondary (cross-flow) flow patterns corre-

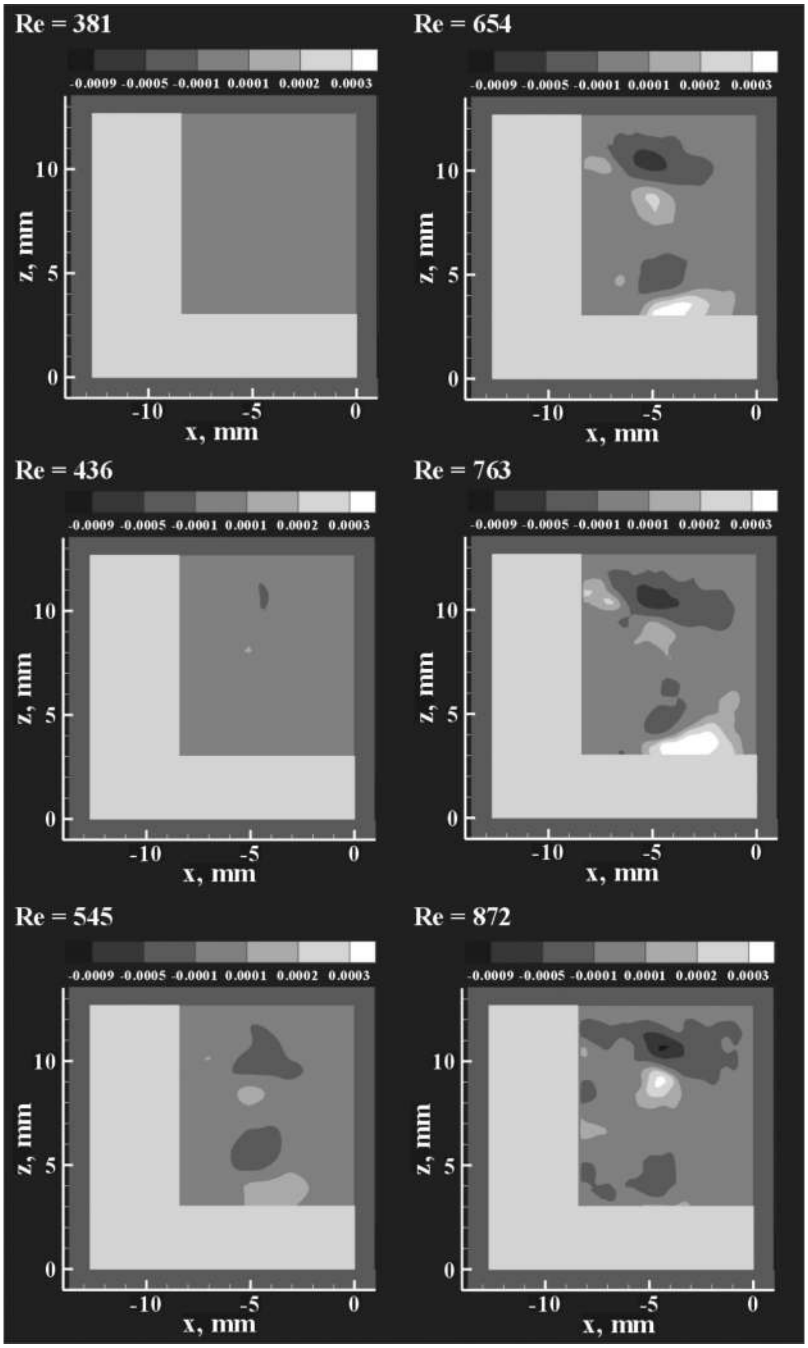

Fig. 13 Patterns of Reynolds stress correlation in the cross-flow plane

sponding to the three time instants represented in Fig. 7. The large-scale Dean vortex pair still remains a dominant feature of the secondary flow. However, the shape and circulation values of the Dean vortices fluctuate with time reflecting the unsteady nature of the flow. The distinguishing feature of the secondary flow at this high-flow-rate regime is the presence of the smaller-scale vortices that are induced by the stronger fluctuating Dean vortex pair. These vortices do not follow the symmetrical flow pattern observed at the low-flow-rate regime. Instead, they appear intermittently throughout the flow field and exhibit a range of scales and circulation values due to mutual induction as well as the interaction with the Dean vortices and the channel walls.

The transition between the low- and high-flow-rate regimes is also observed in the ratio of the maximum primary and secondary velocity and vorticity, which correspond to the streamwise and cross-flow planes, respectively. The variation of the maximum velocity and vorticity ratios with the Reynolds number is shown in Fig. 9. For both velocity and vorticity, the ratio increases with increasing Reynolds number prior to the transition, while decreasing following the transition. This trend indicates that prior to the transition, the circulation of the (secondary) Dean vortices increases until the maximum velocity and vorticity reaches the values observed in the streamwise plane just prior to the transition. Following the transition to the unsteady high-flow-rate mode, the secondary flow circulation and momentum are distributed over a progressively wider range of the smaller-scale vortices, which are observed in the cross-flow plane. This distribution of energy results in the observed decrease in the maximum secondary velocity and vorticity relative to the corresponding parameters in the primary flow plane.

3.2 Averaged Flow Patterns

3.2 Averaged Flow Patterns. The averaged fluctuation amplitude of the separated flow in the U-bend is represented by patterns of root-mean-square velocity fluctuations $|\underline{V}|_{\mathrm{rms}}$. Figure 10 shows distribution of $|\underline{V}|_{\mathrm{rms}}$ in the streamwise plane for six different values of Reynolds number. For the lower flow rates ($\mathrm{Re} < 381$), the flow is essentially steady, and no significant velocity fluctuations were detected. As the Reynolds number increases, the fluctuations become more pronounced, and the $|\underline{V}|_{\mathrm{rms}}$ magnitudes increase. The highest values are associated with the recirculation zones at the outer corners of the U-bend and with the separated flow region originating from the first (downstream) inner corner. At the higher flow rates ($\mathrm{Re}=763$ and $\mathrm{Re}=872$), flow oscillations in the channel downstream of the U-bend can be observed. In this region, the local peak of the $|\underline{V}|_{\mathrm{rms}}$ values corresponds to the reattachment of the flow to the inner wall.

Patterns of root-mean-square velocity fluctuations in the cross-flow plane are shown in Fig. 11. Similarly to the streamwise plane, the amplitude of the oscillations increases with increasing flow rate. This is manifested by the increase in the peak values of $|\underline{V}|_{\mathrm{rms}}$. The highest magnitudes correspond to the counter-rotating Dean vortices. Although these vortices remain the dominant feature of the secondary flow patterns, their location and shape fluctuate as the Reynolds number increases. Moreover, the smaller-scale secondary vortices that appear intermittently at higher flow rates contribute to the increase of the $|\underline{V}|_{\mathrm{rms}}$ levels in the cross-flow plane.

The level of turbulent activity and mixing is often characterized by the Reynolds stress correlation $\langle u'v' \rangle$, where u' and v' are the *fluctuating* velocity components in the x and y directions. The Reynolds stress patterns are presented in Fig. 12, and show the same general trend with respect to increasing Reynolds number as the patterns of root-mean-square velocity fluctuations $|\underline{V}|_{\mathrm{rms}}$ (Fig. 10). The dominant flow structures that contribute to the largest values of $\langle u'v' \rangle$ are the recirculation cells in the outer corners of the U-bend and the separated flow zone originating from the first (downstream) inner corner. In addition, at $\mathrm{Re}=763$ and $\mathrm{Re}=872$, elevated levels of $\langle u'v' \rangle$ in the channel downstream of the U-bend indicate the increase in the background turbulence levels in this region.

Figure 13 shows patterns of Reynolds stress correlation $\langle u'w' \rangle$ in the cross-flow plane. Each of the counter-rotating Dean vortices corresponds to two adjacent regions of elevated $\langle u'w' \rangle$ of the opposite sign. In fact, the magnitudes of $\langle u'w' \rangle$ associated with the intermittent smaller-scale vortices that are present at higher Reynolds numbers are small in comparison with the organized $\langle u'w' \rangle$ corresponding to the Dean vortices. This finding again emphasizes the dominant role of the natural instability of the Dean vortex structure over the background turbulence in the cross-flow plane.

4 Concluding Remarks

Through the application of PIV, a detailed understanding of the flow characteristics in a U-shaped flow channel was acquired. The 180 deg sharp turn, utilized to simulate the first two passes of a serpentine fuel cell flow channel, provided information on the onset of instability in laminar flow at increasing Reynolds numbers as well as the secondary flow at the midpoint of the turn. The flow information was characterized in terms of the instantaneous and time-averaged representations of the velocity, streamline topology, and vorticity contours.

At $\mathrm{Re} \leqslant 381$, the flow in the bend was time independent and was stable downstream from the bend. The time independent nature of the flow in the bend was seen in both the streamwise and cross-flow planes. At $\mathrm{Re} \geqslant 436$, however, the flow in the bend was clearly time dependent in both the streamwise and cross-flow planes and was unstable downstream from the bend.

The secondary flow at the midpoint of the turn appeared to contain four major vortices. Due to optical inaccessibility in the channel, it was not possible to confirm the existence of six vortices observed by Mees [11] in a channel with a 180 deg sharp turn.

The focus of this study has been the characterization of the flow structure, secondary motion, and transition to unsteadiness. These fluid dynamic features are expected to have a significant impact on mass transfer. The ratio of secondary to primary motion was found to decrease after the transition. This suggests that enhanced mixing in the cathode (air) flow channel of a fuel cell could be achieved by designing a serpentine channel such that transition occurs around the Reynolds number corresponding to “design” point operation. Further investigation of mixing and possible mass transfer enhancement, including direct concentration measurements in electrochemically active fuel cells, will be the subject of future work.

ACKNOWLEDGMENTS

This work was performed with a Discovery grant from the Natural Sciences and Engineering Research Council of Canada.

References

[1] Wang, L., Husar, A., Zhou, T., and Liu, H., 2003, “A Parametric Study of PEM Fuel Cell Performances,” Int. J. Hydrogen Energy, **28**(11), 1263–1272.

[2] Nguyen, P. T., Berning, T., and Djilali, N., 2004, “Computational Model of a PEM Fuel Cell With Serpentine Gas Flow Channels” J. Power Sources, **130**(1-2), 149–157.

[3] Dean, W. R., 1928, “Fluid Motion in a Curved Channel,” Proc. R. Soc. London, Ser. A, **121**, 402–420.

[4] Hawthorne, W. R., 1951, “Secondary Circulation in Fluid Flow,” Proc. R. Soc. London, Ser. A, **206**, 374–387.

[5] Agrawal, Y., Talbot, L., and Gong, K., 1978, “Laser Anemometer Study of Flow Development in Curved Circular Pipes,” J. Fluid Mech., **85**, 497–518.

[6] Olson, D. E., and Snyder, B., 1985, “The Upstream Scale of Flow Development in Curved Circular Pipes,” J. Fluid Mech., **150**, 139–158.

[7] Lin, J. Y., and Tarbell, J. M., 1980, “An Experimental and Numerical Study of Periodic Flow in a Curved Tube,” J. Fluid Mech., **100**, 623–638.

[8] Berger, S. A., and Talbot, L., 1983, “Flow in Curved Pipes,” Annu. Rev. Fluid Mech., **15**, 461–512.

[9] Humphrey, J. A. C., Taylor A. M. K., and Whitelaw, J. H., 1977, “Laminar Flow in a Square Duct of Strong Curvature,” J. Fluid Mech., **83**, 509–527.

[10] Bara, B., Nandakumar, K., and Masliyah, J. H., 1992, “An Experimental and Numerical Study of the Dean Problem: Flow Development Towards Two-Dimensional Multiple Solutions,” J. Fluid Mech., **244**, 339–376.

[11] Mees, P. A. J., Nandakumar, K. and Masliyah, J. H., 1996, “Instability and Transitions of Flow in a Curved Square Duct: The Development of Two Pairs of Dean Vortices,” J. Fluid Mech., **314**, 227–246.

[12] Gauthier, G., Gondret, P., Thome, H., and Rabaud, M., 2001, “Centrifugal Instabilities in a Curved Rectangular Duct of Small Aspect Ratio,” Phys. Fluids, **13**, 2831–2834.

[13] Chintada, S., Ko, K. H., and Anand, N. K., 1999, “Heat Transfer in 3-D Serpentine Channels with Right-Angle Turns,” Numer. Heat Transfer, Part A, **36**, 781–806.

[14] Mochizuki, S., Murata, A., Shibata, R., and Yang, W. J., 1999, “Detailed Measurements of Local Heat Transfer Coefficients in Turbulent Flow Through Smooth and Rib Roughened Serpentine Passages with a 180 Degrees Sharp Bend,” Int. J. Heat Mass Transfer, **42**, 1925–1934.

[15] Choi, J. M., and Anand, N. K., 1993, “Heat-Transfer in a Serpentine Channel with a Series of Right-Angle Turns,” Numer. Heat Transfer, Part A, **23**, 189–210.